AD-A165 796 NEUTRON DIFFRACTION CHARACTERIZATION OF TUNGSTEN-NICKEL-IRON ALLOYS(U) ARMY ARMAMENT RESEARCH AND DEVELOPMENT CENTER DOVER NJ ARMAME.. 1/1

UNCLASSIFIED H J PRASK ET AL. FEB 86 ARAED-TR-85015 F/G 7/4 NL

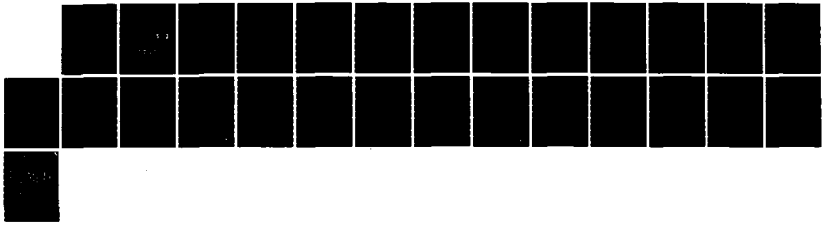

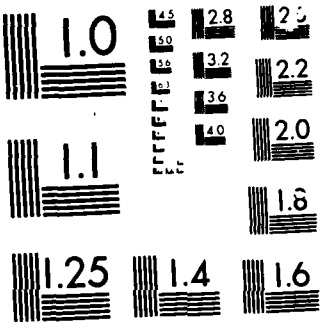

MICROCOPY RESOLUTION TEST CHART

(12)

AD

AD-E401 461

AD-A165 796

TECHNICAL REPORT ARAED-TR-85015

NEUTRON DIFFRACTION CHARACTERIZATION OF TUNGSTEN-NICKEL-IRON ALLOYS

H. J. PRASK
C. S. CHOI

FEBRUARY 1986

US ARMY ARMAMENT MUNITIONS & CHEMICAL COMMAND
ARMAMENT R&D CENTER

U. S. ARMY ARMAMENT RESEARCH AND DEVELOPMENT CENTER
ARMAMENT ENGINEERING DIRECTORATE
DOVER, NEW JERSEY

The views, opinions, and/or findings contained in this report are those of the author(s) and should not be construed as an official Department of the Army position, policy, or decision, unless so designated by other documentation.

Destroy this report when no longer needed. Do not return to the originator.

UNCLASSIFIED

SECURITY CLASSIFICATION OF THIS PAGE *(When Data Entered)*

REPORT DOCUMENTATION PAGE		READ INSTRUCTIONS BEFORE COMPLETING FORM
1. REPORT NUMBER Technical Report ARAED-TR-85015	2. GOVT ACCESSION NO. AD-A165796	3. RECIPIENT'S CATALOG NUMBER
4. TITLE *(and Subtitle)* NEUTRON DIFFRACTION CHARACTERIZATION OF TUNGSTEN-NICKEL-IRON ALLOYS		5. TYPE OF REPORT & PERIOD COVERED Preliminary 1984-5 6. PERFORMING ORG. REPORT NUMBER
7. AUTHOR(s) H. J. Prask and C. S. Choi		8. CONTRACT OR GRANT NUMBER(s)
9. PERFORMING ORGANIZATION NAME AND ADDRESS ARDC, AED Energetics and Warheads Div [SMCAR-AEE] Dover, NJ 07801-5001		10. PROGRAM ELEMENT, PROJECT, TASK AREA & WORK UNIT NUMBERS PROG. ELEMENT: 6.11.01.A PROJECT: 1L161101A91A
11. CONTROLLING OFFICE NAME AND ADDRESS ARDC, IMD STINFO Div [SMCAR-MSI] Dover, NJ 07801-5001		12. REPORT DATE February 1986 13. NUMBER OF PAGES 27
14. MONITORING AGENCY NAME & ADDRESS*(if different from Controlling Office)*		15. SECURITY CLASS. *(of this report)* UNCLASSIFIED 15a. DECLASSIFICATION/DOWNGRADING SCHEDULE

16. DISTRIBUTION STATEMENT *(of this Report)*

Approved for public release; distribution unlimited.

17. DISTRIBUTION STATEMENT *(of the abstract entered in Block 20, if different from Report)*

18. SUPPLEMENTARY NOTES

This project was initiated in 1982 by the Large Caliber Weapon Systems Laboratory, Energetic Materials Division, ARDC.

19. KEY WORDS *(Continue on reverse side if necessary and identify by block number)*

Neutron diffraction
Small-angle neutron scattering
Tungsten-Nickel-Iron alloys
Kinetic energy penetrators
Residual stress
Precipitates
Strain aging

20. ABSTRACT *(Continue on reverse side if necessary and identify by block number)*

Neutron diffraction and small-angle scattering have been employed to elucidate the effect of strain aging on macroscopic properties of tungsten-nickel-iron (W-.07Ni-.03Fe) alloys. The neutron measurements indicate that strain aging causes reduction and redistribution of residual stresses induced by swaging, accompanied by void/precipitate evolution.

DD FORM 1 JAN 73 1473 EDITION OF 1 NOV 65 IS OBSOLETE

UNCLASSIFIED

SECURITY CLASSIFICATION OF THIS PAGE *(When Data Entered)*

CONTENTS

TABLES

FIGURES

INTRODUCTION

Tungsten alloys have been used in kinetic-energy (KE) penetrator munitions because of their high density and ductility, and because of the relative effectiveness and economy of their producibility by means of powder metallurgy techniques. Although a considerable amount of research and testing has been performed on tungsten alloys and penetrators produced therefrom, it appears that optimization has not yet been achieved (see, e.g., ref 1). Part of the reason for this is an inability to correlate all changes in macroscopic mechanical properties and processing parameters with microscopic properties. One example of this is the fact that strain aging after swaging significantly affects certain mechanical properties such as tensile strength and elongation (ref 2), but produces no clear microstructural changes in the material (ref 3).

Neutron scattering is a technique which has the potential for revealing certain structural and materials properties not readily determined by other methods, as has been described previously (refs 4, 5, 6). In the case of tungsten-alloy penetrator materials neutron diffraction is a much more sensitive probe of matrix properties than is x-ray diffraction because of the comparable coherent cross-sections of Ni, Fe, and W in the neutron case (ref 5).

In this paper we present the results of a preliminary investigation of the variation of microscopic properties in unswaged, swaged and strain-aged 90 wt% tungsten- 7 wt% nickel- 3 wt% iron penetrator material as revealed by wide- and small-angle neutron scattering.*

METHOD

Experimental

Two types of neutron instruments were employed: high-resolution neutron diffractometers (HRND) to examine differences in lattice properties of the W and matrix phases of the various samples, and the small-angle neutron scattering (SANS) instrument to determine defect or precipitate differences in the samples. In both cases the samples were totally immersed in the neutron beam. Pertinent instrumental parameters are summarized in table 1.

Samples

The W-.07Ni-.03Fe specimens were obtained from Oak Ridge Y-12 Plant after preparation according to the procedure described in reference 3. Blanks were vacuum annealed at 1050°C for 20 hr (90-0). Specimen 90-24 was 24% cold worked by swaging; specimen 90-24SA was 24% swaged, followed by strain aging for 5 hr at

* Measurements performed at National Bureau of Standards Research Reactor, Gaithersburg, MD.

500°C. Neutron-scattering samples were cut from the blanks and machined into 25.4 mm diameter discs, 1.12 mm thick. Densities of the three discs, measured by R. Schoonover of NBS, agreed to 0.01 g/cm^3 at 17.35 g/cm^3.

Analysis Details

Wide-Angle Diffraction and Strains

The cold-worked samples studied were assumed to contain appreciable levels of residual stress. Macroscopic residual stresses produce strains which cause changes in d-spacings of inter-atomic planes. When averaged in all directions over an entire sample, a range of tensile balanced by compressive stresses produces no net strain and no net change in d-spacing. However, the presence of strains produces a broadening of diffraction peaks, the degree of which is related to the magnitude of stress. Neglecting particle size broadening (ref 7 and references cited therein),

$$W^D_{2\theta'} = 4 \tan^2\theta' \langle e^2 \rangle \qquad (1)$$

where $W^D_{2\theta'}$ is the variance of the broadening in $2\theta'$, θ' is the Bragg angle, and $\langle e^2 \rangle$ is the variance of the lattice strain distribution. Bragg peaks are observed where the Bragg condition, $\lambda = 2d\sin\theta'$, is fulfilled with λ = neutron wavelength. The strain-broadening variance is related to the measured full-width at half-maximum, B, by

$$W^D_{2\theta'} = (B^2 - b_R^2)/8\ln 2 \qquad (2)$$

where b_R is the full-width at half-maximum intensity (FWHM) of the gaussian resolution function.

Some additional information can be obtained about the stress/strain distribution if one examines specific, high-symmetry directions in the sample. With reference to figure 1 the strain in cylindrical geometry is related to stress by (ref 6 and references cited):

$$\begin{aligned} e'_{\phi\Psi} = {} & 1/2\, S_2(hkl)[\sigma_{rr}\cos 2\phi \sin^2\Psi + \sigma_{\theta\theta}\sin\phi^2 \sin^2\Psi \\ & + \sigma_{zz}\cos^2\Psi + \sigma_{r\theta}\sin 2\phi \sin^2\Psi + \sigma_{rz}\cos\phi \sin 2\Psi \\ & + \sigma_{\theta z}\sin\phi \sin 2\Psi] + S_1(hkl)[\sigma_{rr} + \sigma_{\theta\theta} + \sigma_{zz}]. \end{aligned} \qquad (3)$$

In equation 3, e' is the strain measured along $\bar{L}'_3$ at ϕ,Ψ to the sample-fixed coordinates, the σ_{ij} are the residual stress components, and the S_i are "diffraction elastic constants" which depend on the elastic compliances and the

(hkl)-plane. For elastically isotropic solids $1/2S_2(hkl) = (1 + \mu)/E$ and $S_1(hkl) = -\mu/E$ where μ is Poisson's ratio and E is Young's modulus.

In the disc-samples studied $\vec{P}_3$ corresponds to the cylinder axis, and because of the symmetry we assume $\sigma_{r\theta} = 0$.[3] Two high-symmetry directions were examined in the samples: $\Psi = 0°$ (i.e., reflection geometry) and $\Psi = 90°$ (transmission geometry), for which equation 3 becomes

$$e_T' = 1/2\ S_2(hkl)[\sigma_{rr}\cos^2\phi + \sigma_{\theta\theta}\sin^2\phi] + S_1(hkl)[\sigma_{rr} + \sigma_{\theta\theta} + \sigma_{ZZ}] \qquad (4a)$$

and

$$e_R' = 1/2\ S_2(hkl)[\sigma_{ZZ}] + S_1(hkl)[\sigma_{rr} + \sigma_{\theta\theta} + \sigma_{ZZ}]. \qquad (4b)$$

Within this analytical framework one can examine differential volumes within a sample, as we have described in reference 6, to obtain stress as a function of position. However, in the present work we have examined each sample disc, totally immersed in the neutron beam.

We average the strains over the entire volume and assume that the stresses are independent of ϕ; then for each phase we have

$$\bar{e}_T = \frac{1}{v}\int r dr dz\{\tfrac{1}{2}S_2[\pi\sigma_{rr} + \pi\sigma_{\theta\theta}] + 2\pi S_1[\sigma_{rr} + \sigma_{\theta\theta} + \sigma_{zz}]\} \qquad (5a)$$

and

$$\bar{e}_R = \frac{1}{v}\int r dr dz\{2\pi[\tfrac{1}{2}S_2\sigma_{zz} + S_1(\sigma_{rr} + \sigma_{\theta\theta} + \sigma_{zz})]\} \qquad (5b)$$

from which

$$\bar{e}_T - \bar{e}_R = \frac{1}{v}\int r dr dz[\sigma_{rr} + \sigma_{\theta\theta} - 2\sigma_{zz}]\pi(\tfrac{1}{2}S_2). \qquad (6)$$

Under the assumption that swaging and strain-aging change neither the compositions of the constituent phases nor the crystal structures, the change in the "stress integral" in equation 6 can be examined for a given reflection as a function of thermo-mechanical processing.

Recalling that strain is

$$e = (d - d_o)/d_o$$

then

$$\bar{e}_T - \bar{e}_R = (d_T - d_R)/d_o$$

$$= d_T/d_R - 1.$$

Equation 6 can be rewritten as

$$\Sigma = (d_T/d_R - 1)/\pi(\tfrac{1}{2}S_2) \qquad (7)$$

where

$$\Sigma = \frac{1}{V}\int r dr dz[\sigma_{rr} + \sigma_{\theta\theta} - 2\sigma_{zz}]. \tag{8}$$

It should be mentioned that although the samples are in overall equilibrium with respect to stress, each phase considered separately may contain a non-zero integrated stress.

Small-Angle Scattering

Small-angle neutron scattering is a technique which is analogous to small-angle x-ray scattering; however, neutrons penetrate, typically, several orders of magnitude more material than comparable wavelength x-rays. Perhaps more important is the fact that, unlike for x-rays, scattering cross-sections of neighboring elements (e.g., carbon and nitrogen) or even different isotopes of the same element (e.g., hydrogen and deuterium) can be quite different, leading to precipitate, void, or defect "contrasts" not possible with x-rays. A comprehensive review of basic theory and applications is presented in references 5 and 8.

The physical parameters of importance in the SANS regime are the number of scattering particles, N_p, their volume, V_p, the scattering-length density contrast, $\Delta\rho$, the scattering vector, q, and the particle radius of gyration, R_G, with

$$q = \frac{4\pi}{\lambda}\sin\theta' \tag{9}$$

and

$$\Delta\rho_{ij} = A_o\left\{\frac{(\Sigma b_i)\rho_i}{(MW)_i} - \frac{(\Sigma b_j)\rho_j}{(MW)_j}\right\}. \tag{10}$$

Here, A_o is Avogadro's number, (Σb_i) is the average scattering length of atoms in the i^{th} medium, ρ_i is the average density of the i^{th} medium, and $(MW)_i$ is the average molecular weight in the i^{th} medium. In the present (preliminary) work we assume that if defects, precipitates or voids are present, they are spherical in shape and monodisperse.

Following the classic work of Guinier, and Porod, outlined in reference 8, it has been customary to consider two extremes in qR_G for analysis. For $qR_G \lesssim 1.2$ the Guinier approximation is valid and the scattered intensity in solid angle Ω is given by

$$I(q,\Omega) = \frac{N_p}{V}V_p^2(\Delta\rho)^2 e^{-q^2R_G^2/3} \tag{11}$$

where V is the volume of sample in the neutron beam. For very large q (empirically for $qR_G \geq 3$) the scattered intensity is given by

$$I(q,\Omega) = \frac{2\pi(\Delta\rho)^2}{q^4} \frac{S}{V} \qquad (12)$$

where S is the total surface area of the spherical scatterers in V.

To examine the regions appropriate to equations 11 and 12, measurements are made by masking-out the transmitted incident beam with an absorber such as cadmium. Analyses are then made for the smallest-angle scattering data judged to be unaffected by the central beam and the largest-angle scattering data for which reasonable intensity is observed.

Very recently Berk and Hardman-Rhyne (ref 9) and Hardman-Rhyne et al. (ref 10) have developed and applied a method for analysis of the broadening of the direct beam, including multiple scattering effects, to extend the sensitivity of SANS to particles up to micrometers in size. The reader is referred to the references cited for the formalism of this "beam-broadening" analysis method.

RESULTS

Wide-Angle Diffraction

Texture

In the present work a full characterization of sample textures was not made. However, least-squares fits of gaussian profiles to Bragg reflections yield integrated intensities for those reflections. Results for the three samples for transmission and reflection geometries are compared in table 2.

The measurements show that swaging dramatically changes the preferred orientation of both tungsten and matrix grains in the specimen, which is expected. In addition, the difference in relative intensities for 90-0 reflection peaks and 90-0 transmission peaks indicates that significant texture is present even before swaging. The more important aspect of these data is the comparison of 90-24 and 90-24S intensities. Within the estimated uncertainties, no difference is observed in W(hkl) intensities for 90-24 and 90-24S samples either in reflection or transmission. This confirms our premise that the blanks from which the 90-24 and 90-24S samples were prepared were essentially identical. However, the matrix phase intensities, particularly for the reflection measurements, show definite changes after strain-aging.

Lattice Parameters and Stresses

The sensitivity of neutron diffraction to structural changes in each phase of the sample is illustrated by the comparison with x-ray diffraction in figure 2. Crystallographically, the tungsten phase is body-centered cubic (Im3m) and the matrix phase is face-centered cubic (Fm3m).

In table 3 measured d-spacings for tungsten and matrix phases are shown for reflection and transmission measurements. The fact that the d-spacings are different in the reflection and transmission measurements indicates the presence of measurable residual stresses (equation 6). This prevents a precise determination of cell constants for the tungsten and matrix phases of the different samples. In table 4 approximate lattice constants obtained from simple averages of pairs of d-spacing measurements are shown. No differences due to thermo-mechanical treatment are observed.

A change in residual stress distribution produced by thermo-mechanical treatment can be inferred from equation 7. However, this requires the diffraction elastic constants, $S_i(hkl)$, for each phase. Since the tungsten phase is almost pure tungsten, the compliances tabulated in reference 11 and the method described in reference 12 yield reliable values. In the case of the matrix phase the elastic constants are not known, so as a first approximation the diffraction elastic constants for pure nickel are employed (ref 12). The measured d-spacings of table 4 are used to obtain the results for Σ presented in table 5.

Related to but independent of the above is the analysis of peak broadening to extract the variance of the lattice strain distribution through equation 1. Measured (gaussian) resolution is subtracted from the total (gaussian) profiles as described earlier. In this case, root-mean-square (r.m.s.) strains are obtained without reference to stresses producing them. Values from the neutron data are presented in table 6. For clarity, in both table 5 and table 6, weighted averages of results for identical reflections are presented, as appropriate. No systematic differences were observed in measured FWHM for reflection and transmission data for individual reflections.

It should be emphasized that Σ and $\langle e^2 \rangle^{1/2}$ reflect different aspects of the residual stress distribution. If residual stresses are present, broadening of the Bragg peaks and a finite $\langle e^2 \rangle$ will be observed. The stress integral, Σ, averages over $(\sigma_{rr} + \sigma_{\theta\theta} - 2\sigma_{zz})$ which could be zero even if stresses are present. On the other hand Σ depends on the distribution of stresses so that for two samples Σ can change even if $\langle e^2 \rangle$ is the same for each. This type of behavior is observed for the W-phase of the present samples.

The W-phase in the 90-0 sample shows no measurable strain broadening. After swaging significant r.m.s. strains are present while $\Sigma(90\text{-}24) \neq 0$. After strain-aging, the magnitude of r.m.s. strain is essentially unchanged, whereas the distribution of stress changes appreciably. In the matrix phase Σ and $\langle e^2 \rangle$ appear to change in parallel. A significant increase in stress occurs on swaging, and strain-aging appears to cause some stress relaxation and redistribution. The fact that Σ of M(hhh) and M(200) reflections differ consistently by about a factor of 2 indicates that the elastic constants, and S_2 derived from them, are very different from those of pure nickel.

Small-Angle Diffraction

Guinier/Porod Regions

In figure 3 two representations of the noncenter SANS data, circularly averaged, for the 90-24S sample are shown. (We use "noncenter" to indicate that the transmitted incident beam is absorbed by a cadmium beam stop in contrast to center, "beam-broadening" data.) It is interesting that without additional information one might attempt to analyze the ln I(q) versus q^2 data as a composite of linear, "Guinier" components arising from several particle radii. For example, three distinct distributions each containing particles with a single radius (e.g., R_1 = 30, R_2 = 90, R_3 = 190Å) would fit the data very well. However, examination of the ln I(q) versus ln q representation shows that almost all of the data follows the Porod law. This indicates that the Guinier region consists of only a few data points, analysis of which is not practicable.

The Porod region is analyzed for the three samples by means of equation 12. Under the assumption that the scatterers are spherical and of the same type in each sample, ratios of scatterer total surface area can be obtained from the Porod-region data. For spherical scatterers, the total surface area is proportional to ϕ/r where r is the radius of the scattering spheres and ϕ is the fractional volume of scatterers in the total sample volume in the beam. The ratio ϕ(90-0)/r(90-0):ϕ(90-24)/r(90-24):ϕ(90-24S)/r(90-24S) is 0.57:1.00:0.98 from the Porod analysis.

Beam-Broadening Region

The width increase of the direct beam is dependent on scatterer-matrix contrast, $\Delta\rho$, fractional scatterer volume, ϕ, scatterer radius, r, and wavelength. For the present samples only λ = 12.2 and 14.0Å show sufficient broadening for useful analysis. Results for two possibilities are presented: W-precipitates in the matrix, and voids in the matrix. Here, "W-precipitates" refers to W which dissolves in the matrix at the sintering temperature, but precipitates out at ambient temperature--not the starting tungsten powder particles ($r \geq 10$ μm). For each wavelength an r versus ϕ curve is calculated from the Berk model (ref 9), which is determined by the measured beam broadening and the known parameters. For a given sample, the intersection of the curves for each wavelength is taken to determine ϕ and r for that sample. This is illustrated in figure 4. The uncertainties shown are determined by calculating, at the cross-over ϕ value, the particle radii at $\pm\sigma$ from the nominal beam-broadening value. It is clear that the relatively large uncertainties prohibit a meaningful comparison of properties of 90-24 and 90-24S material. Nevertheless, the ϕ/r ratios from the beam-broadening data are 0.59:1.0:0.85 for 90-0:90-24:90-24S, in agreement with the Porod-region analysis if uncertainties are taken into account.

It should be emphasized that figure 4 represents six data points; that is, beam broadening at two wavelengths for three samples. Despite the uncertainties, it is clear that the particle size obtained, r ~ 0.18μm, is consistent with the

noncenter (Porod) analysis. Also, the beam-broadening could be due to about 3% of the matrix volume being occupied by W precipitate or by about 1% of the matrix volume being occupied by voids. A similar analysis assuming voids in tungsten led to a volume fraction of voids which was unrealistically large. Transmission electron microscope results reported by Jones have shown the presence of precipitates in the matrix portion of W/Ni/Fe penetrators (ref 13).

RECOMMENDATIONS

1. The possibility that strain aging relieves residual stresses in the two-phase W-alloy material should be examined in detail in intact penetrators with differential energy-dispersive neutron diffraction, as described in reference 6.

2. The SANS characterization of defects in the matrix phase should be performed definitively by:

a) extension of beam-broadening measurements to longer wavelengths;

b) extension of Porod-region measurements to larger q values with better signal to background.

3. Several samples should be used for the above-described measurements. Where possible, strain aging should be performed in-situ so that sample to sample variations do not mask the effects of thermo-mechanical treatment.

REFERENCES

1. "Second Conference on High-Density Kinetic Energy Penetrator Materials," Technical Report AMMRC SR 81, AMMRC, Watertown, MA, 1981.

2. T. C. Myhre, "Effects of Swaging and Aging on Mechanical Properties of Tungsten, Seven Percent Nickel, Three Percent Iron Alloy," in Technical Report AMMRC SR 81, AMMRC, Watertown, MA, 1981, pp 133-142.

3. E. H. Lee and T. C. Myhre, "Interim Report of 90W-7Ni-3Fe Alloy TEM Examination," Technical Report Y/PG-2286, Oak Ridge Y-12 Plant, Oak Ridge, TN, February 1980.

4. C. S. Choi, H. J. Prask, and S. F. Trevino, "Nondestructive Investigation of Texture by Neutron Diffraction," J. Appl. Cryst, vol 12, 1979, pp 327-331.

5. C. J. Glinka, H. J. Prask, and C. S. Choi, "Neutron Diffraction and Small-Angle Scattering as Nondestructive Probes of the Microstructure of Materials," in Mechanics of Nondestructive Testing (ed. W. W. Stinchcomb), 1980, Plenum Press, NY, pp 143-164.

6. H. J. Prask and C. S. Choi, "NDE of Residual Stress in Uranium by Means of Neutron Diffraction," J. Nucl. Matls., vol 126, 1984, pp 124-131.

7. H. P. Klug and L. E. Alexander, "Crystallite Size and Lattice Strains from Line Broadening," in X-Ray Diffraction Procedures for Polycrystalline and Amorphous Materials (2nd. Ed.), 1974, Wiley Interscience, NY, pp 618-708.

8. J. R. Weertman, "Identification by Small Angle Neutron Scattering of Microstructural Changes in Metals and Alloys," in Nondestructive Evaluation. Microstructure Characterization and Reliability (ed. O. Buck and S. Wolf), 1980, Metallurgical Society of AIME, pp 147-168.

9. N. F. Berk and K. A. Hardman-Rhyne, "Characterization of Alumina Powder Using Multiple Small Angle Neutron Scattering, I: Theory," J. Appl. Cryst., in press.

10. K. Hardman-Rhyne, N. F. Berk, and E. R. Fuller, Jr., "Microstructural Characterization of Ceramic Materials by Small Angle Neutron Scattering Techniques," J. Res. N.B.S., vol 89, 1984, pp 17-34.

11. J. Turley and G. Sines, "The Anisotropy of Young's Modulus, Shear Modulus and Poisson's Ratio in Cubic Materials," J. Phys. D: Appl. Phys., vol 4, 1971, pp 264-271.

12. F. Bollenrath, V. Hauk, and E. H. Müller," Zur Berechnung der Vielkristallinen Elastizitätskonstanten aus den Werten der Einkristalle," Z. Metallkde., vol 58, 1967, pp 76-82.

13. P. N. Jones, "The Effect of Post-Sintering Mechanical and Thermal Treatments on the Microstructure and Properties of Liquid-Phased Tungsten Alloys," in Technical Report AMMRC SR 81, AMMRC, Watertown, MA, 1981, pp 29-40.

Table 1. Instrument characteristics

Instrument	Wavelength(s)	FWHM-resolution
HRND-1	1.542 A	0.296° [a]
HRND-6	2.428	0.395° [a]
SANS	7.0	$6.2 \times 10^{-3} A^{-1}$ [b]
	12.2	$3.6 \times 10^{-3} A^{-1}$ [b]
	14.0	$3.2 \times 10^{-3} A^{-1}$ [b]

[a] Full-width at half-maximum in 2θ measured for W(110).

[b] Full-width at half-maximum in momentum transfer, Q, measured at $Q = 0$.

Table 2. Integrated intensities of selected Bragg peaks[a]

	Reflection			Transmission		
Bragg Peak[b]	94-0	94-24	94-24S	94-0	94-24	94-24S
W(110)	326[c,d]	666	673	149[e]	111	113
W(200)	98	17	19	41	16	16
W(211)	295	93	93	112	61	58
W(220)	132	126	122	43	16	17
M(111)	23	1000	932	374	68	72
M(200)	17	54	65	--[f]	13	18
M(220)	186	52	60	11	53	53
M(311)	17	195	153	1000	79	55
M(222)	--[f]	183	165	158	9	9

[a]These data were obtained with a relatively low resolution diffractometer.

[b]M = Matrix.

[c]Reflection intensities normalized to M(111).

[d]Uncertainties range from 1% (strong reflections) to 10% (weak reflections).

[e]Transmission intensities normalized to M(311).

[f]Too weak to analyze.

Table 3. Measured d-spacings

Reflection-Instrument	d-spacing (Å) R(90-0)[a]	T(90-0)[a]	R(90-24)	T(90-24)	R(90-24S)	T(90-24S)
W(110)-1[b]	2.23607(5)[e]	2.23612(16)	2.23602(16)	2.23607(11)	2.23575(11)	2.23607(11)
W(110)-6	2.23602(6)	2.23584(9)	2.23614(12)	2.23617(9)	2.23587(12)	2.23614(9)
M(111)[d]-1	[c]		2.07167(9)	2.07018(9)	2.07171(5)	2.07081(5)
M(111)-6	2.07173(5)	2.07128(10)	2.07165(10)	2.07021(12)	2.07188(10)	2.07073(10)
M(222)-1	[c]		1.03594(2)	1.03520(6)	1.03616(3)	1.03553(3)
M(200)-6	1.79423(10)	1.79275(17)	1.79623(12)	1.79243(14)	1.79631(9)	1.79306(10)

[a] R = reflection, T = transmission.

[b] HRND-1 of table 1.

[c] Unscanned or weak.

[d] M(hkl) = hkl reflection of matrix phase.

[e] Standard deviation in last significant figure (e.g. 2.23612(16) = 2.23612 ± 0.00016).

Table 4. Approximate cell constants

	A(Å)		
Phase sample	90-0	90-24	90-24S
W	3.162	3.162	3.162
M	3.587	3.587	3.588

Table 5. Volume-averaged net stress, Σ

Reflection	Σ (Arbitrary Stress Units)		
	90-0	90-24	90-24S
W(110)	-4.1 ± 4.5	1.0 ± 5.0	13.2 ± 4.7
M(111)	-13.6 ± 3.4	-44.5 ± 3.0	-28.7 ± 1.7
M(222)	*	-44.8 ± 3.8	-38.1 ± 2.6
M(200)	-33.4 ± 4.4	-85.6 ± 4.1	-73.2 ± 3.0

*Weak or not scanned.

Table 6. Strains from peak broadenings

Reflection	$\langle e^2 \rangle^{1/2} \times 10^4$		
	90-0	90-24	90-24S
W(110)	~ 0	8.6 ± 1.2	8.8 ± 0.9
M(111)	7 ± 4	17.8 ± 0.4	16.2 ± 0.5
M(222)	*	16.8 ± 0.7	15.9 ± 0.7
M(200)	16.1 ± 2.2	29.3 ± 0.5	26.3 ± 0.4

*Weak or not scanned.

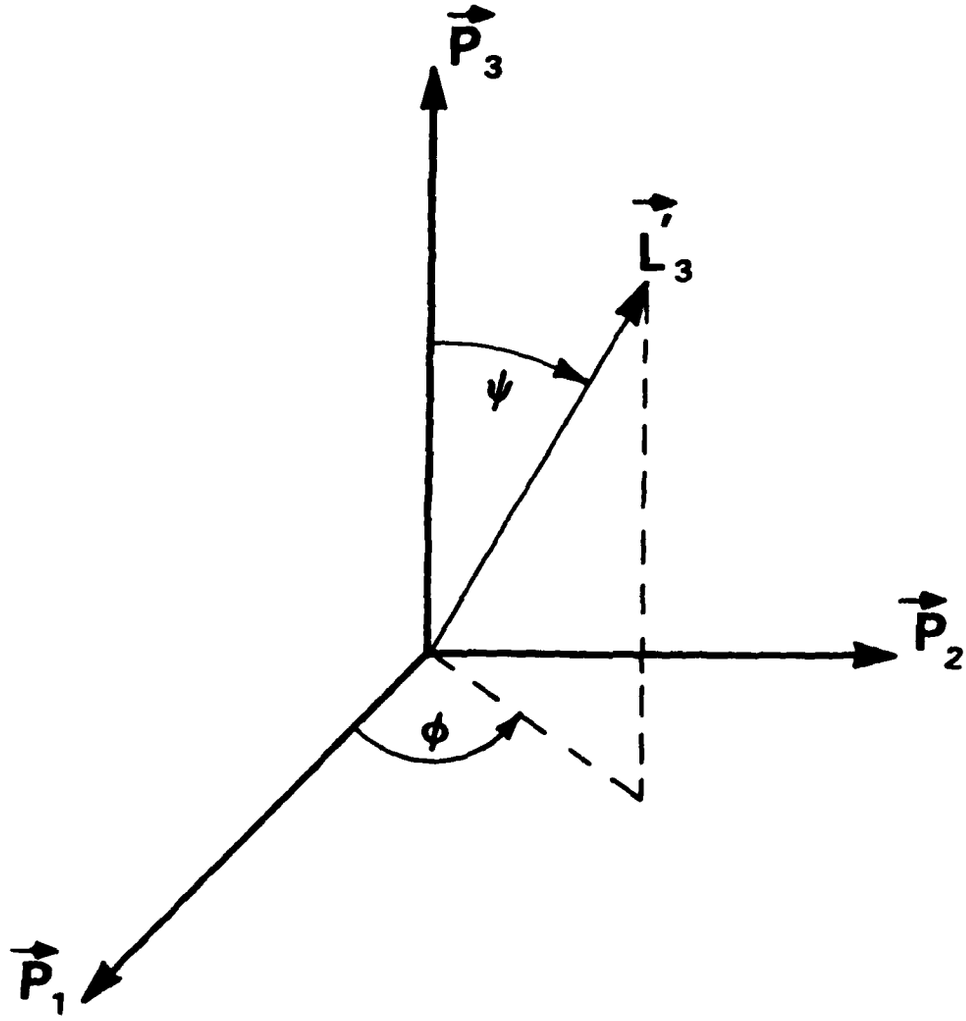

$\vec{P}_i$ = sample-fixed coordinates

$\vec{L}_3$ = wave-vector transfer direction

Figure 1. Coordinate system for stress measurements in cylindrical samples

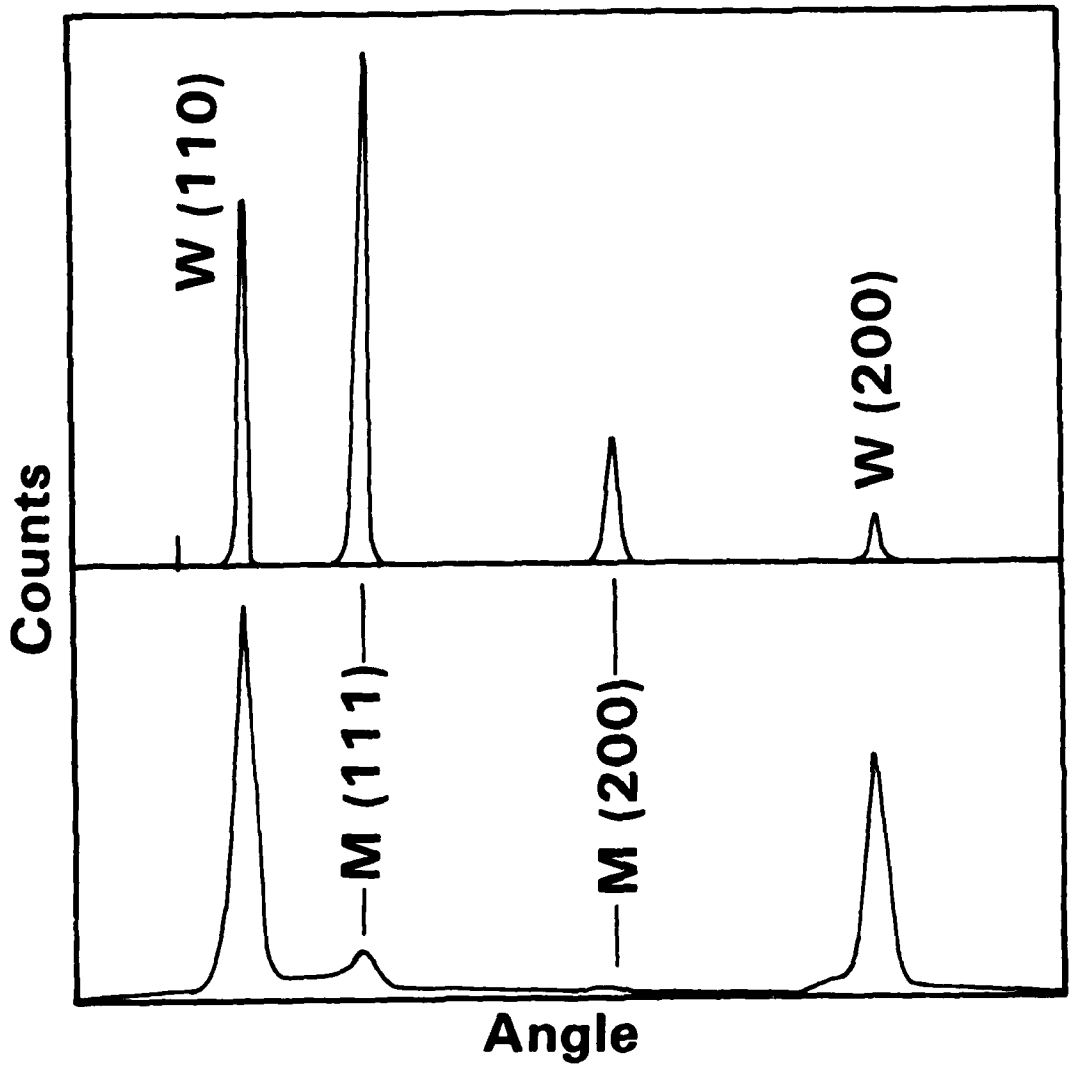

Upper Curve: Combined neutron data from HRND-1 and HRND-6
Lower Curve: Molybdenum K-α x-ray pattern

Figure 2. Comparison of relative sensitivities of x-ray and neutron diffraction techniques to tungsten and matrix components of sample 90-24 (reflection)

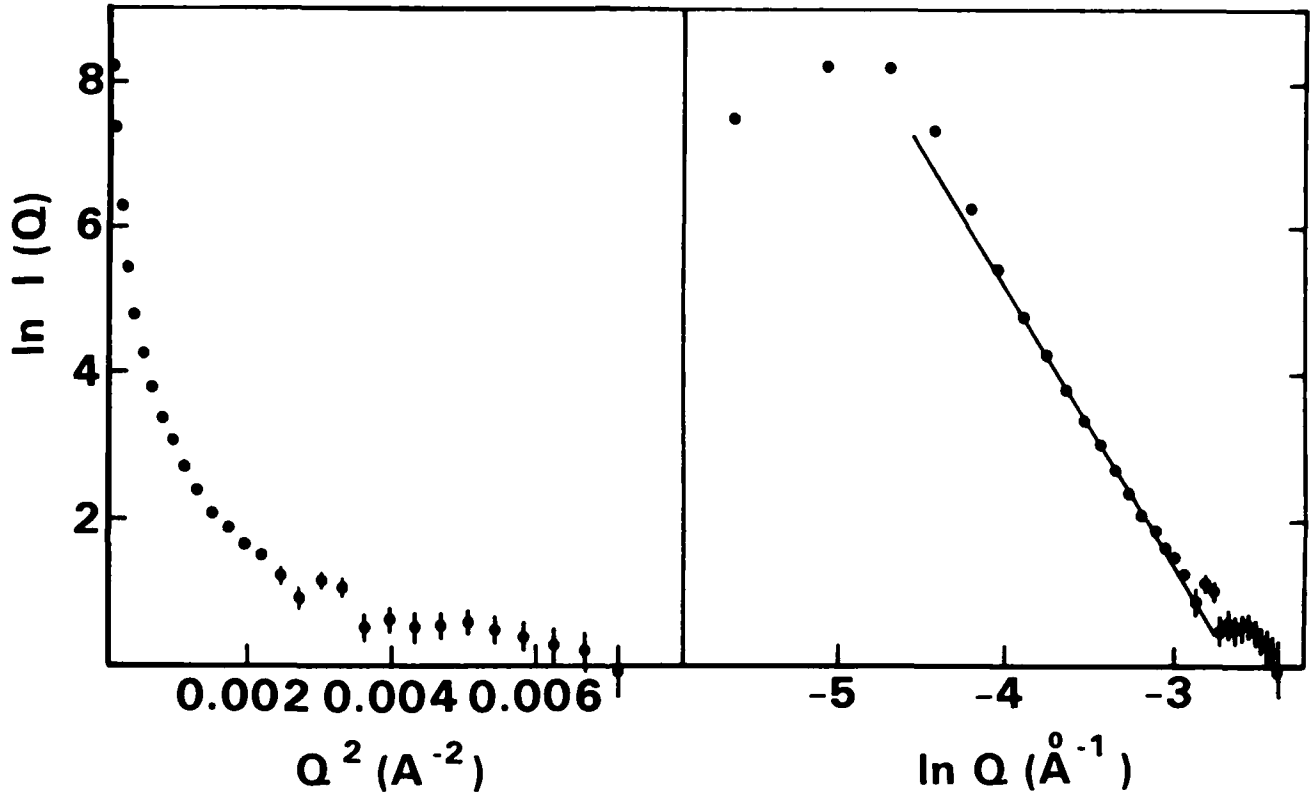

Straight line (right figure) = Porod Law

Figure 3. SANS data for 90-24S plotted in two forms

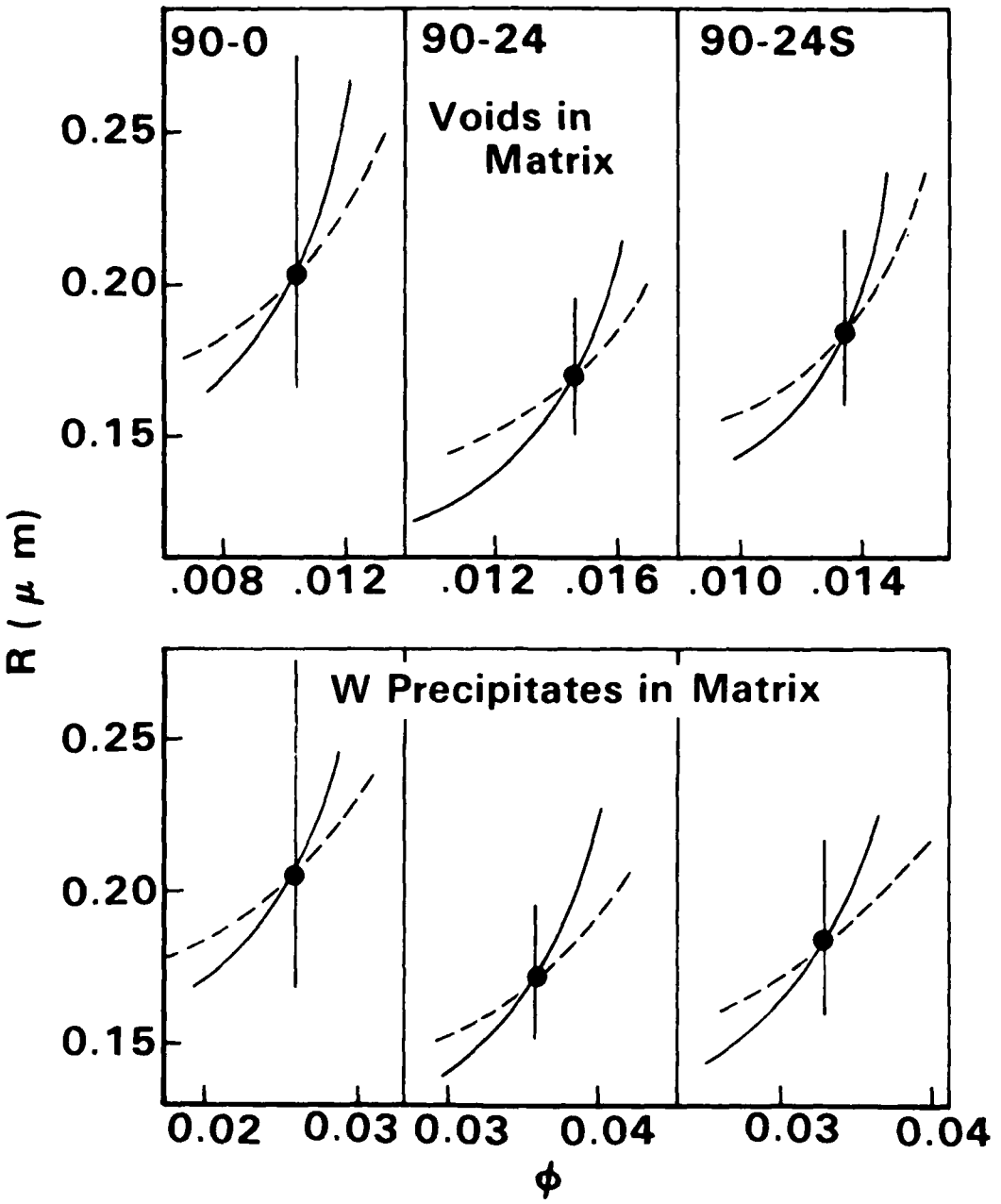

Dashed Curves: $\lambda = 12.2\text{Å}$

Solid Curves: $\lambda = 14.0\text{Å}$

Figure 4. SANS beam-broadening measurements analyzed following reference 11

DISTRIBUTION LIST

Commander
Armament Research and Development Center
U.S. Army Armament, Munitions and Chemical Command
ATTN: SMCAR-AEE, J. Lannon
Word Processing Office (3)
SMCAR-AEE-W, N. Slagg
F. Owens
H. Prask (10)
C. Choi (10)
SMCAR-AET, E. Bloore
F. Witt
SMCAR-FSM, E. Barriers
B. Konrad
W. Sharpe
SMCAR-MSI (5)
Dover, NJ 07801-5001

Commander
U.S. Army Armament, Munitions and Chemical Command
ATTN: AMSMC-GCL(D)
AMSMC-QAT(D), C. Knutsen
Dover, NJ 07801-5001

Administrator
Defense Technical Information Center
ATTN: Accessions Division (12)
Cameron Station
Alexandria, VA 22304-6145

Director
U.S. Army Materiel Systems Analysis Activity
ATTN: AMXSY-MP
Aberdeen Proving Ground, MD 21005-5066

Commander
Chemical Research and Development Center
U.S. Army Armament, Munitions and Chemical Command
ATTN: SMCCR-SPS-IL
Aberdeen Proving Ground, MD 21010-5423

Commander
Chemical Research and Development Center
U.S. Army Armament, Munitions and Chemical Command
ATTN: SMCCR-RSP-A
Aberdeen Proving Ground, MD 21010-5423

Director
Ballistic Research Laboratory
ATTN: AMXBR-OD-ST
AMXBR-TBD, W. Bruchey
D. Dietrich
F. Grace
Aberdeen Proving Ground, MD 21005-5066

Chief
Benet Weapons Laboratory, CCAC
Armament Research and Development Center
U.S. Army Armament, Munitions and Chemical Command
ATTN: SMCAR-CCB-TL
Watervliet, NY 12189-5000

Commander
U.S. Army Armament, Munitions and Chemical Command
ATTN: SMCAR-ESP-L
Rock Island, IL 61299-6000

Director
U.S. Army TRADOC Systems Analysis Activity
ATTN: ATAA-SL
White Sands Missile Range, NM 88002

HQDA
ATTN: DAMA-ART-M
DAMA-CSM
DAMA-ZA
Washington, DC 20310

Commander
US Army Materiel Command
ATTN: AMCPM-GCM-WF
5001 Eisenhower Avenue
Alexandria, VA 22304

Commander
US Army Materiel Command
ATTN: AMCDRA-ST
5001 Eisenhower Avenue
Alexandria, VA 22333-0001

Project Manager
Tank Main Armament Systems
ATTN: AMCPM-TMA, K. Russell - 120
AMCPM-TMA-105
AMCPM-TMA-120
Dover, NJ 07801-5001

END
FILMED
4-86
DTIC